PHYSICAL REVIEW E VOLUME 52, NUMBER 3 SEPTEMBER 1995

Field behavior of an Ising model with competing interactions on the Bethe lattice

Marcelo H. R. Tragtenberg
Departamento de Física, Universidade Federal de Santa Catarina, Campus Universitário, Trindade, Caixa Postal 476, 88040-900 Florianópolis, Santa Catarina, Brazil

Carlos S. O. Yokoi
Instituto de Física, Universidade de São Paulo, Caixa Postal 66318, 05389-970 São Paulo, São Paulo, Brazil

(Received 23 May 1994; revised manuscript received 19 May 1995)

We consider an Ising model with competing interactions on a Bethe lattice in the presence of a magnetic field. In the infinite-coordination limit, the problem reduces to the study of a two-dimensional mapping. We study in detail the properties of this mapping with particular emphasis on the location of the stable periodic orbits, corresponding to commensurate structures of the model, on the field-temperature plane for different strengths of the competing interactions. We develop some efficient numerical procedures for this purpose. We also investigate the existence of strange attractors on the model in the presence of a field.

PACS number(s): 05.45.+b, 05.50.+q, 64.70.Rh

I. INTRODUCTION

It is well known that the solution of the Ising model on a Bethe lattice of coordination number z, formed by the sites deep within the Cayley tree, is equivalent to the Bethe-Peierls approximation of the model on a crystal lattice of the same coordination number [1]. In particular, in the infinite-coordination limit $z \to \infty$ the model on the Bethe lattice becomes equivalent to the mean-field approximation. In a pioneering work Vannimenus [2] studied an Ising model with competing interactions between the nearest and next-nearest-neighbor spins on a Bethe lattice of coordination number $z = 3$ as an analog of the axial next-nearest-neighbor Ising ANNNI [3], model on a tree. Yokoi, Oliveira, and Salinas [4] considered the infinite-coordination limit $z \to \infty$ of the model introduced by Vannimenus. They found a phase diagram that was remarkably similar to that of the ANNNI model, and detected the possibility of chaotic structures in certain regions of the diagram. The fractal character of the attractor associated with the chaotic phase was confirmed by the calculation of the Hausdorff dimension [5]. The possibility of chaotic phases on this deterministic model is interesting in view of the existence of spin-glass phases on the Bethe lattice with random bonds, which has been studied extensively [6–8]. In this respect, we mention that the chaotic phase found in this model was studied from the point of view of the spin-glass theory and was shown to exhibit a spin-glass character [9].

The similarity of results obtained for models defined on Cayley trees and on crystal lattices is a strong motivation for the study of models on trees, since the statistical mechanics on trees presents many simplifying aspects that are absent in models defined on crystal lattices. An attractive feature of the models defined on trees is that they can be formulated as *dissipative* mapping problems, which allows us to borrow the techniques and vocabulary of the theory of dynamical systems [10]. Actually, the models on crystal lattices can also be formulated as *conservative* mapping problems, but the approach does not lend itself to a simpler solution of the problem because the metastable configurations correspond to unstable orbits of the mapping [11]. However, in the case of the models on trees, the attractors of the dissipative mapping are naturally related to the modulated structures deep within the tree.

In this paper we study the field behavior of the model introduced by Vannimenus in the infinite-coordination limit $z \to \infty$. This constitutes the counterpart on trees of the study of the ANNNI model in the presence of a field. The latter problem has been considered by various authors [12–14]. However, no detailed mean-field phase diagram of the modulated region, such as that provided by Selke and Duxbury [15] for zero field, seems to be available. Such a work would probably entail a rather large amount of computational labor, and we hope that the detailed study presented here for the tree will retain enough features of the model on the lattice to be a useful guide for future works. We mention that the Vannimenus model augmented with third-neighbor intershell and nearest-neighbor intrashell interactions on a Bethe lattice of coordination $z = 3$ has been considered in the presence of a field [16], but no detailed study of the modulated region has been reported.

The plan of the paper is as follows. In Sec. II, we define the model and derive the relevant two-dimensional mapping. In Sec. III, we analyze the ground state of the model in a field. In Sec. IV, we study the stability of the paramagnetic or fixed point solutions of the mapping in the presence of a field. In Sec. V, we introduce numerical methods for finding the stability regions of the commensurate phases or periodic orbits of the mapping. In Sec. VI, we report the result of numerical calculations and display the relevant field-temperature phase diagrams. In Sec. VII, we discuss the overlapping of stability regions of distinct periodic orbits with the same period, corresponding to commensurate phases of the same wave number but different structures. In Sec. VIII, we show that periodic orbits with different periods may also be stable in the same regions of the phase diagram. We also discuss the occurrence of strange attractors. Finally we summarize our findings in Sec. IX.

II. FORMULATION OF THE PROBLEM

The Cayley tree is a graph with no cycles and endowed with a hierarchical structure. Each site of the tree has degree, or coordination z, except for the boundary sites, which have a degree of 1. The boundary sites form the first shell. A given site in the nth shell is connected to one vertex in the $(n+1)$th shell and to $z-1$ vertices in the $(n-1)$th shell, as illustrated in Fig. 1 for the case $z=3$. The Ising model on the Cayley tree is given by the Hamiltonian.

$$\mathcal{H} = -\sum_{ij} J_{ij}\sigma_i\sigma_j - H\sum_i \sigma_i, \tag{1}$$

where $\sigma_i = \pm 1$ and H is the magnetic field. In the model introduced by Vannimenus [2] the coordination of the tree is $z=3$ and J_{ij} is equal to $J_1 > 0$ if i and j are nearest-neighbor sites, and equal to J_2 if they are next-nearest-neighbor sites belonging to different shells. We are concerned with the properties of the Cayley tree deep within the graph, known as the Bethe lattice [1]. The local properties of the tree in a shell are related recursively to the local properties in the previous two shells [2,17,18]. These recursion relations can be written as a three-dimensional mapping. The local properties deep within the lattice, that is, the properties of the Bethe lattice, are naturally related to the attractors of the mapping. In the infinite-coordination limit $z \to \infty$, keeping $\mathcal{J}_1 = zJ_1$ and $\mathcal{J}_2 = z^2 J_2$ finite, there is a considerable simplification because then the recursion relations can be written as a two-dimensional mapping. In the limit $z \to \infty$ the local magnetization in the nth shell, M_n, is given by the recursion relation [4]

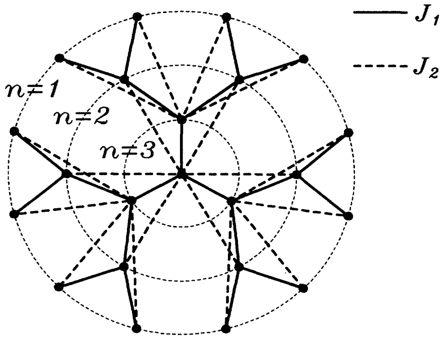

FIG. 1. Cayley tree with coordination $z=3$ and $N=3$ shells. The first (J_1) and second (J_2) neighbor interactions are indicated by solid bold and dashed bold lines, respectively.

$$M_n = \tanh\left[\frac{1}{kT}(\mathcal{J}_1 M_{n-1} + \mathcal{J}_2 M_{n-2} + H)\right]. \tag{2}$$

In what follows we will set

$$k = 1, \quad \mathcal{J}_1 = 1, \quad \mathcal{J}_2 = -\kappa. \tag{3}$$

Defining $x_n \equiv M_{n-1}$ and $y_n \equiv M_n$ the recursion relation (2) can be rewritten as a two-dimensional dissipative mapping

$$\begin{aligned}\boldsymbol{x}_{n+1} = \begin{pmatrix} x_{n+1} \\ y_{n+1}\end{pmatrix} &= \begin{pmatrix} y_n \\ \tanh[\frac{1}{T}(y_n - \kappa x_n + H)]\end{pmatrix} \\ &= \boldsymbol{F}(\boldsymbol{x}_n).\end{aligned} \tag{4}$$

The choice of the initial point of the mapping (x_1, y_1) is equivalent to the choice of the boundary conditions on the magnetizations of the first and second shells of the tree.

After a sufficient number of iterations the points of the mapping settle near one of the attractors of the mapping. An important characterization of the attractor is furnished by the Lyapunov exponents [10], which measure the mean exponential rate of convergence or divergence of the trajectories surrounding the attractor. The Lyapunov characteristic exponents are defined by

$$\lambda_i = \lim_{N\to\infty} \frac{1}{N} \ln|\Lambda_i| \quad (i = 1, 2), \tag{5}$$

where Λ_i are the eigenvalues of the matrix

$$\boldsymbol{L} = \boldsymbol{J}(\boldsymbol{x}_N)\boldsymbol{J}(\boldsymbol{x}_{N-1})\cdots\boldsymbol{J}(\boldsymbol{x}_2)\boldsymbol{J}(\boldsymbol{x}_1), \tag{6}$$

formed by the products of the Jacobian matrices $\boldsymbol{J}(\boldsymbol{x}_n)$ of $\boldsymbol{F}$ computed at the points $\boldsymbol{x}_n$ of the attractor

$$\begin{aligned}\boldsymbol{J}(\boldsymbol{x}_n) &= \left.\frac{\partial \boldsymbol{F}}{\partial \boldsymbol{x}}\right|_{\boldsymbol{x}=\boldsymbol{x}_n} \\ &= \begin{pmatrix} 0 & 1 \\ -\frac{\kappa}{T}(1 - y_{n+1}^2) & \frac{1}{T}(1 - y_{n+1}^2)\end{pmatrix}.\end{aligned} \tag{7}$$

For convenience we order the Lyapunov exponents according to their size,

$$\lambda_1 \geq \lambda_2. \tag{8}$$

We found that the following types of attractors are realized for the mapping (4): (a) *fixed points*, corresponding to paramagnetic or ferromagnetic phases with $\lambda_2 < \lambda_1 < 0$; (b) *periodic cycles* of period Q or *Q-cycles*, corresponding to commensurate phases, with $\lambda_2 < \lambda_1 < 0$; (c) *aperiodic orbits*, corresponding to incommensurate phases, with $\lambda_1 = 0$ and $\lambda_2 < 0$; and finally (d) *strange attrac-*

tors, corresponding to chaotic phases, with $\lambda_1 > 0$ and $\lambda_2 < 0$. It may happen that, for given values of T, κ, and H, the points of the mapping converge to different attractors depending on the choice of the initial point. In this case the regions of stability of these attractors overlap. Physically it means that the phase that is realized deep within the tree depends on the boundary conditions set up in the first and second shells of the tree. In such cases we will say that these phases are *co-stable*, and the region of joint stability of these attractors will be called the *co-stability* region. The main purpose of this work is to determine the regions of stability of the attractors of types (a) and (b) and build the phase diagrams in the T-H plane for different values of the competing strength κ. We also study the occurrence of strange attractors of type (d).

III. THE GROUND STATE OF THE MODEL

In the limit of zero temperature the recursion relation (2) takes the form

$$M_n = \mathrm{sgn}(M_{n-1} - \kappa M_{n-2} + H), \tag{9}$$

where $\mathrm{sgn}(x) = -1$, 0, or 1 according to whether $x < 0$, $x = 0$, or $x > 0$, respectively. This recursion relation can be easily analyzed. The stability regions of different attractors are shown in Fig. 2. In region A, defined by $H < 1 - \kappa$ and $H > \kappa - 1$, the fixed points (1,1) and $(-1,-1)$ are stable and can be reached from suitable initial conditions. The fixed points (1,1) and $(-1,-1)$ correspond to ferromagnetic phases with all the shell magnetizations parallel and antiparallel to the field, respectively, which we will indicate by + and −. Therefore, in this region the phases + and − are co-stable. In region B, characterized by $H \geq 1 - \kappa$ and $H > \kappa - 1$, only the fixed point (1,1) corresponding to the phase + is stable. Conversely, in region C, defined by $H \leq \kappa - 1$ and $H < 1 - \kappa$, only the fixed point $(-1,-1)$ corresponding to the phase − is stable. Finally, in region D, characterized by $H < \kappa - 1$ and $H > 1 - \kappa$, the only stable attractor is the four-cycle corresponding to the (2,2) antiphase $\cdots ++--++--\cdots$; that is, two shells with magnetizations parallel to the field followed by two shells with magnetizations antiparallel to the field, and so on successively.

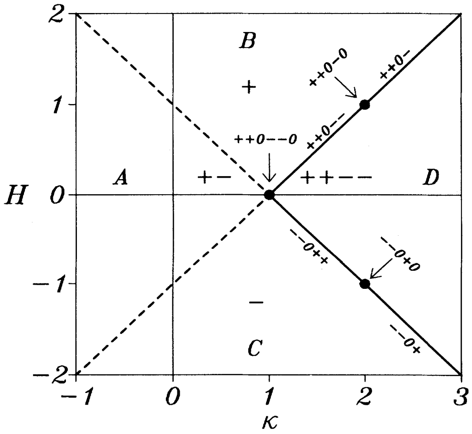

FIG. 2. Zero temperature phase diagram showing the ground states of the model.

Contrary to the ANNNI model [12], the lines $H = \kappa - 1$ and $H = 1 - \kappa$, for $\kappa \geq 1$ do not constitute multiphase lines in the sense that the ground state is infinitely degenerate. In fact, at the point $\kappa = 1$ and $H = 0$, the only attractor is the six-cycle $\cdots ++0--0++0--0\cdots$. Along the line $H = \kappa - 1$ the only attractor is a five-cycle $\cdots ++0--++0--\cdots$ for $1 < \kappa < 2$, a five-cycle $\cdots ++0-0++0-0\cdots$ for $\kappa = 2$, and finally it is a four-cycle $\cdots ++0-++0-\cdots$ for $\kappa > 2$. Identical results, except for a global inversion of the magnetizations, are found along the line $H = 1 - \kappa$. Although these lines are not infinitely degenerate, at nonzero temperatures many, possibly infinite, phases converge to these lines. It is with this understanding that we will refer to these lines as multiphase lines.

IV. REGION OF STABILITY OF THE PARAMAGNETIC PHASE

The paramagnetic or ferromagnetic phase correspond to the fixed point $\boldsymbol{x}^* = (x^*, y^*)$ of the mapping (4), which has the form

$$x^* = y^* = M, \tag{10}$$

where M is the local magnetization given by

$$M = \tanh\left[\frac{(1-\kappa)M + H}{T}\right]. \tag{11}$$

The eigenvalues of the Jacobian matrix computed at the fixed point are given by

$$\begin{matrix}\Lambda_2 \\ \Lambda_1\end{matrix} = \frac{1-M^2}{2T}\left[1 \pm \left(1 - \frac{4\kappa T}{1-M^2}\right)^{1/2}\right]. \tag{12}$$

The stability limit of a given fixed point is then determined by the condition

$$\max\{|\Lambda_1|, |\Lambda_2|\} = 1, \tag{13}$$

which gives, as a function of T and κ, the magnetization M_c for this fixed point at the boundary of stability. The corresponding field can be obtained from Eq. (11),

$$H_c = (\kappa - 1)M_c + T\tanh^{-1}M_c, \tag{14}$$

which determines the boundary of the region of stability in the H-T plane. For the case $\kappa < \frac{1}{2}$ Eq. (13) has the solutions

$$M_c^{\pm} = \pm\left(1 - \frac{T}{1-\kappa}\right)^{1/2}. \tag{15}$$

We will denote $H_c^+ = H_c(M_c^+)$ and $H_c^- = H_c(M_c^-)$. These curves have the form shown in Fig. 3. The meaning of these curves is as follows. There is always a stable

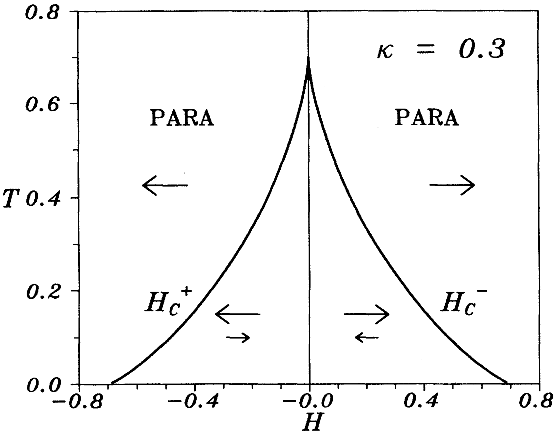

FIG. 3. Stability region of the paramagnetic phase for $\kappa = 0.3$. Inside the tent-shaped region there is a co-stability of two phases, with magnetizations parallel and antiparallel to the field, as indicated by the arrows.

fixed point with magnetization parallel to the field. In addition, for temperatures below $T = 1 - \kappa$ there may be also a fixed point with magnetization antiparallel to the field that becomes unstable at the curves $H = H_c^{\pm}$. Therefore in the region delimited by the curves $H_c^{\pm}$ there are two distinct fixed points with magnetizations of opposite sign that are co-stable. For the case $\kappa > \frac{1}{2}$ we find

$$M_c^{\pm} = \pm \left(1 - \frac{T}{\kappa}\right)^{1/2} . \tag{16}$$

The curves $H_c^{\pm}$ corresponding to the magnetizations given by (16) are shown in Fig. 4 for $1 > \kappa > \frac{1}{2}$. There are no stable fixed points in the shaded bubble-shaped region delimited by the curves $H_c^{\pm}$, whereas in the tent-shaped region below there are two fixed points with opposite magnetizations that are co-stable. Figure 5 shows the curves $H_c^{\pm}$ for $\kappa > 1$. There are no stable fixed points in the shaded region delimited by the curves $H_c^{\pm}$, and outside this region there is only one fixed point with magnetization parallel to the field.

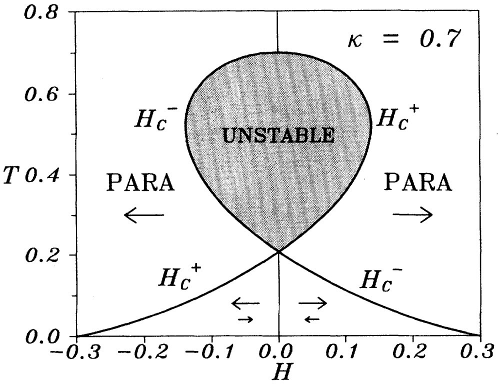

FIG. 4. Stability region of the paramagnetic phase for $\kappa = 0.7$. Inside the tent shaped region there is a co-stability of two phases, with magnetizations parallel and antiparallel to the field, as indicated by the arrows. Inside the shaded bubble-shaped region the paramagnetic phase is unstable.

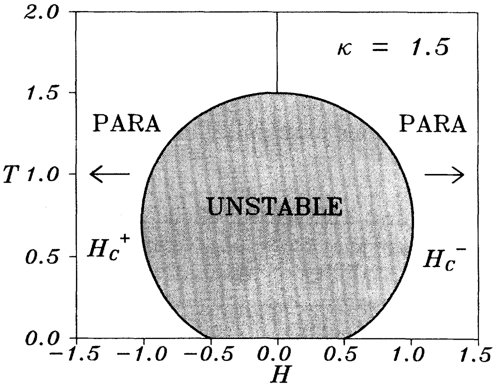

FIG. 5. Stability region of the paramagnetic phase for $\kappa = 1.5$. Inside the shaded bubble-shaped region the paramagnetic phase is unstable.

The eigenvalues Λ_1 and Λ_2 at the stability boundary are complex numbers of modulus one for $\kappa > \frac{1}{2}$. The phase q_c of these complex eigenvalues, called the critical wave number, is given by

$$\cos q_c = \frac{1 - M_c^2}{2T} = \frac{1}{2\kappa}. \tag{17}$$

The wavelength of the modulated structure just outside the boundary of stability of the paramagnetic phase is $2\pi/q_c$. It is noteworthy that q_c depends only on κ, being independent of T and H, a feature common to the ANNNI model in the mean-field approximation [12].

V. METHODS FOR DETERMINING THE EXISTENCE REGION OF COMMENSURATE PHASES

For $\kappa > \frac{1}{2}$, there are regions in the H-T plane where periodic cycles of period Q are stable attractors of the mapping (4). Physically, these Q-cycles are associated with the emergence of commensurate modulated structures deep within the tree. In this section we are concerned with the problem of determining the region of stability of these Q-cycles in the H-T plane; that is, to determine the H-T phase diagram of commensurate phases. In principle this is simply a matter of iterating the mapping (4) a sufficient number of times and verifying if the points of the mapping converge to a Q-cycle. This method works satisfactorily for small periods and has been used extensively [4,18]. In fact, it is the simplicity of this method compared to more laborious methods necessary for models on crystal lattices [15] that constitutes one of the attractive features of models defined on trees. However, for long period cycles or close to the stability limit of commensurate phases the convergence of the points of the mapping to the attractor may become quite slow, requiring a prohibitively large computational work. This is a particularly serious drawback for the case of our problem because many commensurate phases become very narrow and we need to build various phase diagrams for different values of κ to have a fairly complete picture of the behavior of the model in the field. In order to overcome these difficulties we developed two alternative approaches that proved to be far superior to the simpleminded iteration of the mapping (4).

A Q-cycle is characterized by the fact that after Q iterations of the mapping (4) one comes back to the starting point, $\boldsymbol{x}_{n+Q} = \boldsymbol{x}_n$. The points of the orbit are therefore the solutions of the equation

$$\boldsymbol{x} = \underbrace{\boldsymbol{F}(\boldsymbol{F}(\cdots\boldsymbol{F}(\boldsymbol{F}(\boldsymbol{x}))\cdots))}_{Q\ \text{times}} = \boldsymbol{F}^{(Q)}(\boldsymbol{x}). \tag{18}$$

Obviously, in a Q-cycle there will be Q distinct solutions to this equation corresponding to the Q points of the orbit. The nonlinear system of two equations (18) can be solved by the Newton method. Let $\boldsymbol{x}_0^{(i)}$ be a trial solution near one of the points of the Q-cycle, and let

$$\boldsymbol{x}_0^{(i+1)} = \boldsymbol{x}_0^{(i)} + \delta\boldsymbol{x}_0^{(i)}. \tag{19}$$

Inserting $\boldsymbol{x}_0^{(i+1)}$ into Eq. (18) and expanding to first order in $\delta\boldsymbol{x}_0^{(i)}$, we find

$$\boldsymbol{x}_0^{(i)} + \delta\boldsymbol{x}_0^{(i)} = \boldsymbol{F}^{(Q)}\left(\boldsymbol{x}_0^{(i)} + \delta\boldsymbol{x}_0^{(i)}\right) \approx \boldsymbol{x}_Q^{(i)} + \boldsymbol{L}\delta\boldsymbol{x}_0^{(i)}, \tag{20}$$

where $\boldsymbol{L}$ is the matrix defined in Eq. (6). Therefore the correction $\delta\boldsymbol{x}_0^{(i)}$ that moves $\boldsymbol{x}_0^{(i)}$ closer to the solution of Eq. (18) is given by

$$\delta\boldsymbol{x}_0^{(i)} = (\boldsymbol{L} - \boldsymbol{I})^{-1}\left(\boldsymbol{x}_0^{(i)} - \boldsymbol{x}_Q^{(i)}\right). \tag{21}$$

We found numerically that the iterative process represented by Eqs. (19) and (21) converges very quickly to one of the points of the orbit if we are in the region where a Q-cycle exists whereas no convergence is observed otherwise. As a criterion for convergence we adopted $\max(|\delta x_0^{(i)}|, |\delta y_0^{(i)}|) < 10^{-9}$, and as the maximum number of iterations we chose 20. Thus, if no convergence were observed within 20 iterations we assumed that there was no Q-cycle. In this way, beginning with one point inside the region of existence of a Q-cycle and one point outside, the boundary was determined by a process of bisection. Needless to say, the convergence of the iterative process depends on the initial point, and the lack of convergence for a given initial point does not necessarily mean that there is no Q-cycle. However, experience shows that such troublesome situations occur only in very small regions of the phase diagram, and that by considering a good sampling of initial conditions one can get reliable results.

In certain regions of the phase diagram there are solutions of Eq. (18) that correspond to *repellors*; that is, unstable Q-cycles with positive Lyapunov exponents. This kind of orbit can never be reached by the iteration of the mapping; in other words, they can never be realized on the Bethe lattice and therefore have no physical interest. Another aspect to be considered is that different initial conditions may converge to different Q-cycles. In these cases, the regions of stability of different Q-cycles overlap, and we say that there is a *co-stability* of different commensurate phases with the same period.

The stability region of commensurate phases becomes very narrow for long periods or close to the transition to the paramagnetic phase. Often the width of these phases becomes smaller than the precision employed in the calculations. The method described previously, which depends on the knowledge of a point inside the region of existence of the phase, cannot be applied in these circumstances. This is a serious limitation because in our problem there are phases that are extremely narrow in the region of interest. We developed an alternative procedure to cope with these cases. Let us define the function

$$\Phi(T, \kappa, H, Q) = \min_{\boldsymbol{x}_0} \parallel \boldsymbol{x}_Q - \boldsymbol{x}_0 \parallel^2, \tag{22}$$

where $\boldsymbol{x}_Q = \boldsymbol{F}^{(Q)}(\boldsymbol{x}_0)$ and $\parallel \boldsymbol{x} \parallel = \parallel (x, y) \parallel = \sqrt{x^2 + y^2}$. The function Φ represents the square of the minimum "distance" between the points $\boldsymbol{x}_0$ and $\boldsymbol{x}_Q = \boldsymbol{F}^{(Q)}(\boldsymbol{x}_0)$, and therefore has the property of vanishing inside the region of existence of a Q-cycle. The two-dimensional minimization in (22) can easily be performed by any of the standard optimization routines. The boundary of the region of existence of the Q-cycle can be determined; for example, using the secant method [19] to find the root of Φ always keeping *outside* the region of existence of a Q-cycle.

Figure 6 shows the zero field T-κ phase diagram of the model obtained using the methods described in this section. The shaded regions are commensurate phases, and the labeling fractions indicate $q/2\pi$. In between these commensurate phases there are possibly an infinite number of other commensurate, as well as incommensurate, phases.

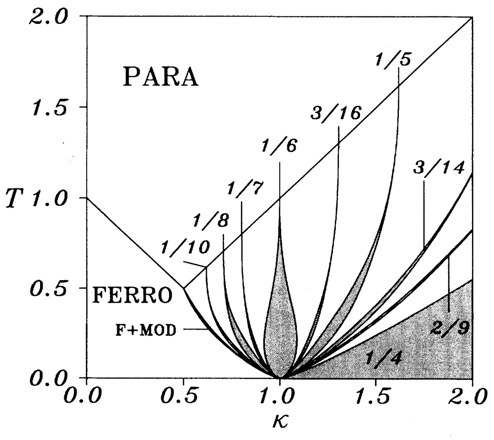

FIG. 6. Zero field T-κ phase diagram. Only the main commensurate phases (shaded regions) are indicated. In the shaded region indicated by F+MOD the ferromagnetic and modulated phases are co-stable.

VI. FIELD-TEMPERATURE PHASE DIAGRAMS

In this section we will present the field-temperature phase diagrams for some representative values of the parameter κ. We emphasize that the methods described in the preceding section were fundamental in constructing these phase diagrams. This work would have been totally impracticable using only the iteration method. In these phase diagrams the commensurate phases are labeled by the reciprocal of wavelength or $q/2\pi$. Many commensurate phases appear only as lines because their widths are too narrow to be resolved at the scale of the figure.

Figures 7 and 8 show the typical phase diagrams for $\kappa < 1$. As a general feature we observe that the modulated phases are stable in the region of instability of the paramagnetic phase determined in Sec. IV, but there is, in addition, a region of co-stability of paramagnetic and modulated phases at low temperatures. The relative extension of this co-stability region is larger the smaller the parameter κ, and has been indicated by light shading in Fig. 7. This co-stability region was determined by iterating the mapping (4) 50 000 times starting from different initial conditions to check the existence of modulated phases. The point where the co-stability region disappears corresponds to the tricritical point, indicated by TCP in these figures.

We observe that the commensurate phases that are present at zero field survive up to rather high fields before folding back. Many of these phases penetrate into the co-stability region after the folding, although some commensurate phases, such as 1/13 in Fig. 7, enter the co-stability region before the folding, and some commensurate phases, such as 1/20 in Fig. 7, are entirely within the co-stability region. Because of the overlapping of all these phases the co-stability region is extraordinarily complex.

Notice that commensurate phases with wave numbers close to q_c, such as 4/43 in Fig. 7 or 5/32 in Fig. 8, tend to follow the paramagnetic-modulated boundary, which is consistent with the fact that q_c given by Eq. (17) is independent of H. We also observe the pinching of some commensurate phases, such as 1/8 in Fig. 8. This effect is related to the co-stability of different commensurate phases with the same wave number, as will be explained in more detail in Sec. VII.

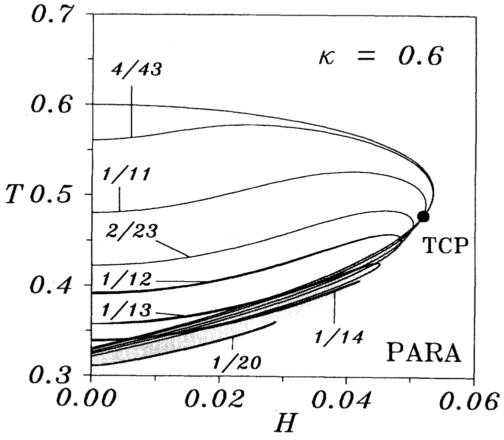

FIG. 7. T-H phase diagram for $\kappa = 0.6$. In the light-shaded region paramagnetic and modulated phases are co-stable. The co-stability region ends at the tricritical point (TCP).

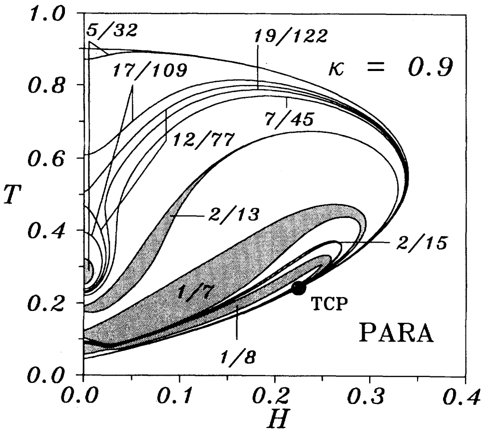

FIG. 8. T-H phase diagram for $\kappa = 0.9$. Observe the existence of disjoint commensurate phases and the pinching of the 1/8 phase. The co-stability region between paramagnetic and modulated phases is too narrow to be visible at the scale of the figure, and ends at the tricritical point (TCP).

The phase diagram of Fig. 8, for κ slightly smaller than 1, shows commensurate phases exhibiting complicated behaviors. For example, in Fig. 8 the phase 5/32 appears in a bubble shaped region at low temperatures, and also as a phase extending to high fields at higher temperatures. Similarly, the phases 17/109 and 12/77 in Fig. 8 appear in annular regions at low temperatures and again as phases extending to high fields at higher temperatures. The existence of disjoint commensurate phases with the same wave number is related to the nonmonotonicity of the wave number as a function of temperature, for given κ, close to the 1/6 phase at zero field. In other words, there are commensurate phases with the same wave number at different temperatures for the same value of κ, as shown in Fig. 9.

Figure 10 shows the T-H phase diagram for the value of κ exactly equal to 1. In the absence of a field the only modulated phase is 1/6. In the presence of a field, although the 1/6 phase fills almost half of the modulated region, there are still many commensurate phases with smaller wave numbers in the region of higher fields. These phases spring up from the multiphase point at $(\kappa, T, H) = (1, 0, 0)$, and resemble the coats of an onion, with the commensurate phases with larger wave numbers surrounding those with smaller wave numbers. The co-stability between modulated and paramagnetic phases disappears, being replaced by a co-stability between different modulated phases in the central region of the onion, as can be seen in Fig. 10, where one observes the overlap between the 1/7 and 1/8 phases.

Figures 11 and 12 show the T-H phase diagram for κ slightly larger than 1. They show how a small increase

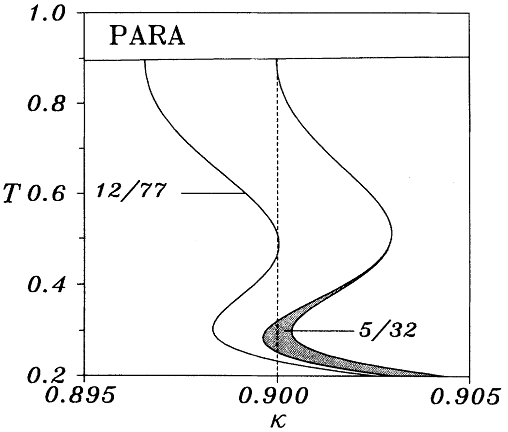

FIG. 9. Detail of the T-κ phase diagram in the neighborhood of $\kappa = 0.9$. The phases 5/32 and 12/77 recur two and three times, respectively, as the temperature is lowered for $\kappa = 0.9$.

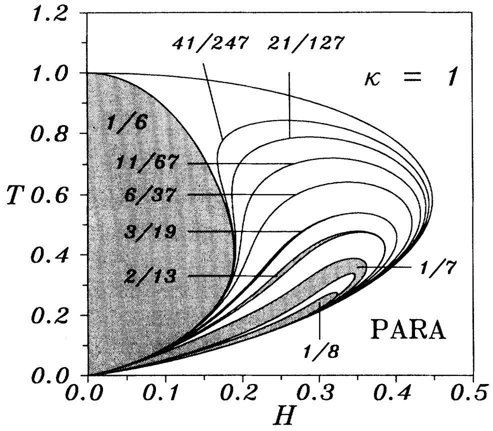

FIG. 10. T-H phase diagram for $\kappa = 1$.

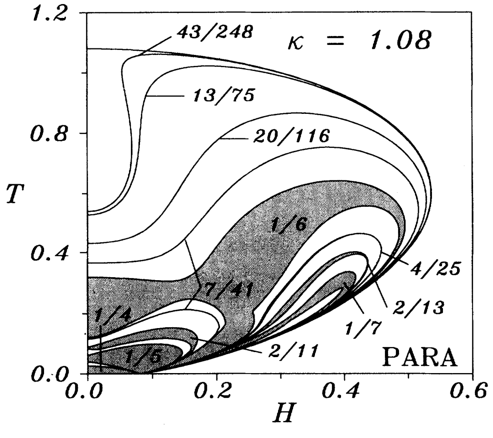

FIG. 11. T-H phase diagram for $\kappa = 1.08$.

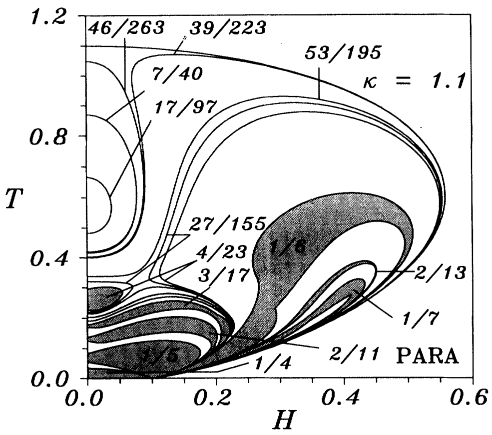

FIG. 12. T-H phase diagram for $\kappa = 1.1$.

in κ changes the phase diagram dramatically. In particular, the phase 1/6 suffers a profound change. In Fig. 11, for $\kappa = 1.08$, we observe that the phase 1/6 develops two tentacles extending to the multiphase point. One of the tentacles surrounds some modulated phases with wave numbers larger than $2\pi(1/6)$, whereas the other surrounds those with wave numbers smaller than $2\pi(1/6)$. For $\kappa = 1.1$, Fig. 12, the phase 1/6 no longer exists for zero field. The phase diagram for $\kappa = 1.1$ is quite complex, showing many commensurate phases existing in disjoint regions. This complexity can again be traced back to the nonmonotonicity of the wave number as a function of temperature, for given κ and $H = 0$, close to the phase 1/6. Also, it is interesting to observe that the phase 4/23 exists in two disconnected regions: a bubble-shaped one, which is an extension of the phase that already exists at zero field, and also as one of the layers of the onion springing up from the multiphase point. Another fact that calls ones attention is the existence of a sharp corner in the lower boundary of the 1/6 phase. This sharp corner is related to the co-stability of two distinct commensurate 1/6 phases, as will be discussed in more detail in Sec. VII.

Figure 13 shows a typical T-H phase diagram for larger

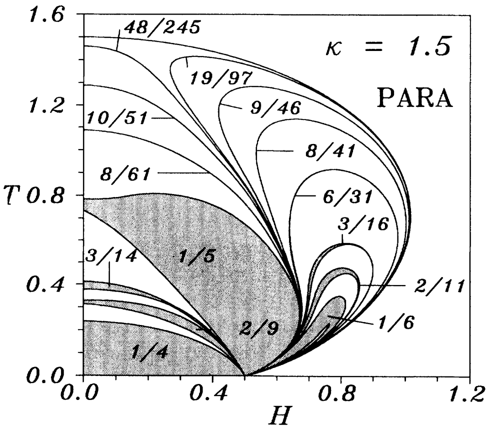

FIG. 13. T-H phase diagram for $\kappa = 1.5$.

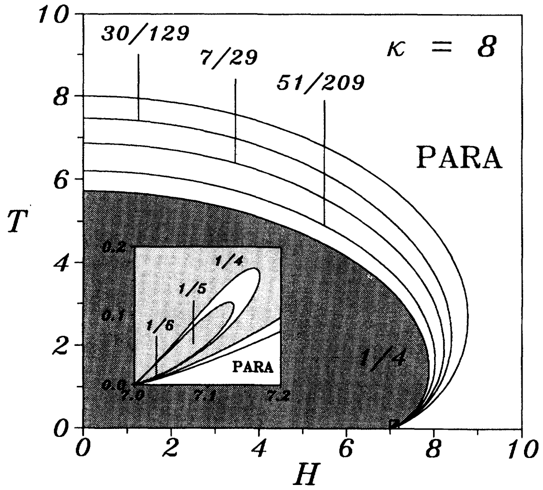

FIG. 14. T-H phase diagram for $\kappa = 8$. The inset shows the detail near the multiphase point.

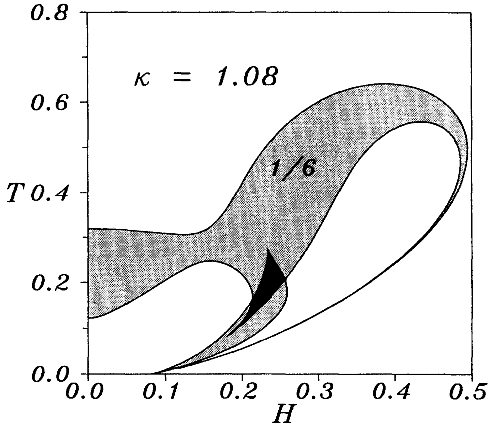

FIG. 15. Region of co-stability of different 1/6 phases (dark-shaded region) for $\kappa = 1.08$.

values of κ. There are two possible behaviors for the modulated phases. Those with wave numbers larger than q_c, which are already present at zero field, survive in the presence of a field and end up at the multiphase point. However, those with wave numbers less than q_c, which are not present at zero field, have the shape of coats of an onion springing up from the multiphase point, with phases with larger wave numbers enveloping those with smaller wave numbers. The modulated phase with $q = q_c$, corresponding to the borderline case, starts at $T = T_c$, $H = 0$ and ends at the multiphase point $T = 0$, $H = \kappa - 1$. It should be mentioned that at the central part of the onion-shaped region many modulated phases with different periods are co-stable.

As the value of the parameter κ further increases, the phase 1/4 becomes increasingly preponderant relative to other modulated phases, as can be seen in Fig. 14. Apparently, the onion-shaped phases have disappeared completely, but actually they still survive in a minute region of the phase diagram, as can be seen in the inset of Fig. 14. In the limit $\kappa \to \infty$ the model can be thought of as being two uncoupled antiferromagnetic Bethe lattices. Therefore, in this limit, the 1/4 phase should be the only remaining phase.

VII. CO-STABILITY OF COMMENSURATE PHASES WITH EQUAL WAVE NUMBERS BUT DIFFERENT STRUCTURES

In the last section we mentioned that some of the commensurate phases show marked changes in the form of their phase boundaries. For example, the sharp corner of the 1/6 phase in Fig. 12 is clearly visible. This aspect of the phase boundaries is related to the co-stability of commensurate phases with the same wave numbers but different structures. Figure 15 shows the region of co-stability of these two types of 1/6 commensurate phases in the T-H phase diagram as a darker shaded region. The co-stability region was determined studying the largest Lyapunov exponents associated with the different attractors of the 1/6 phase.

The co-stability of different structures in the interior of commensurate phases with a given wave number seems to be fairly common, even though they are often not easily revealed by the shape of the phase boundaries. Examples are the phases 2/9 and 3/14 of Fig. 13. A careful investigation shows that there are co-stability regions for small fields in the 2/9 phase and for higher fields in the 3/14 phase, as shown in Fig. 16 as a shaded region. In the case of the 2/9 phase, the different co-stable structures are related, at zero field, by a global inversion of the magnetizations. We expect this kind of co-stability to occur for all other odd period phases at small fields.

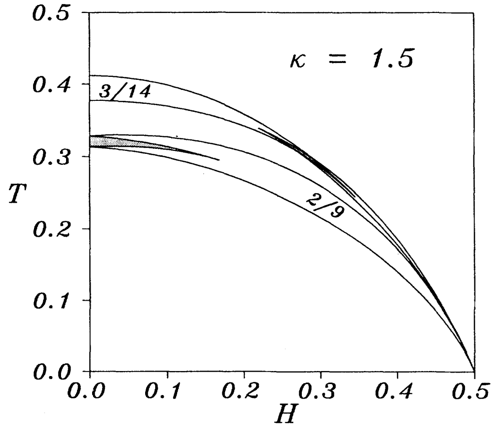

FIG. 16. Regions of co-stability of 2/9 and 3/14 phases with different structures (shaded regions).

VIII. CO-STABILITY OF MODULATED PHASES WITH DIFFERENT WAVE NUMBERS AND STRANGE ATTRACTORS

All the T-H phase diagrams of the model for $\kappa > \frac{1}{2}$ have regions where modulated phases with different periods are co-stable. These regions are relatively small compared to the whole phase diagram, but they are exceedingly complex. It is also in these regions that strange attractors, corresponding to chaotic phases, are present.

For $\kappa \geq 1$ the co-stability of modulated phases with different periods occurs in the central region of the onion-shaped phases. For example, for $\kappa = 1.5$, the co-stability region is located within the 1/6 phase of Fig. 13. Figure 17 shows the 1/6 phase in more detail. There are many, possibly an infinity, of modulated phases which are stable in the central region of the 1/6 phase, but they are not shown. In the light shaded region the 1/6 phase becomes unstable. The study of the largest Lyapunov exponent shows that in this region the six-cycle becomes a repellor with positive Lyapunov exponent, as shown in Fig. 18(b). Moreover, in this region the 12-cycle becomes stable. This process of period doubling continues as the temperature is lowered. Thus, the central region of the stability interval of the 12-cycle becomes unstable, giving place to a 24-cycle, as shown in Fig. 18(c), and so on. Clearly this kind of period doubling is related to the emergence of strange attractors according to one of the routes to chaos [20].

For $\kappa < 1$ there are regions where paramagnetic and modulated phases are costable, as can be seen, for example, in Fig. 7. It is not easy to study the commensurate phases that penetrate into this region. Figure 19 shows what happens to the 1/11 phase. This phase extends upwards from the zero field until it folds itself downwards and turns back. However, this lower branch does not extend very much because it becomes unstable, as shown in the inset of Fig. 19. We found that other commensurate phases show a behavior analogous to the 1/11 phase in the region of co-stability between modulated and paramagnetic phases, although some of them become unstable before the bending occurs.

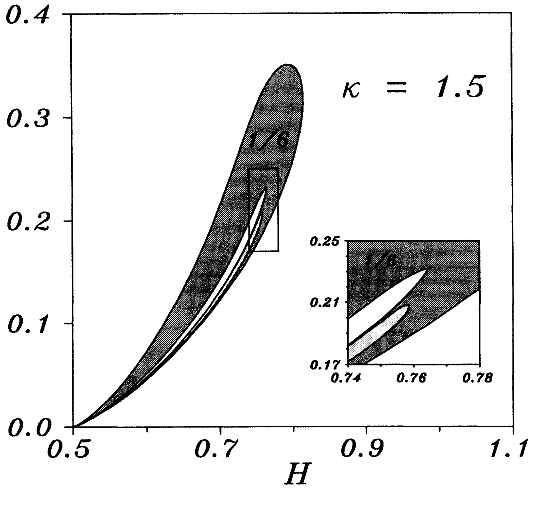

FIG. 17. Detail of the 1/6 phase for $\kappa = 1.5$. In the lighter shaded region the 1/6 phase becomes unstable.

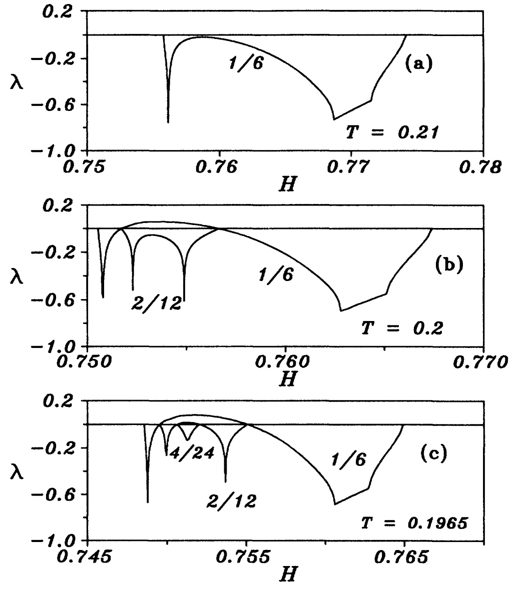

FIG. 18. Lyapunov exponent and period doubling of the 1/6 phase for $\kappa = 1.5$ and different temperatures.

We have found strange attractors in all the regions of co-stability of modulated phases with different periods. It is not our purpose to study these strange attractors in detail, as has been done for the strange attractor found at zero field [5], but merely to point out their existence also in the presence of a field. As an illustration, we consider the strange attractor found for $\kappa = 0.6$. Figure 20 shows the strange attractor found at the point $\kappa = 0.6$, $H = 0.0247$ and $T = 0.35$. The largest Lyapunov expo-

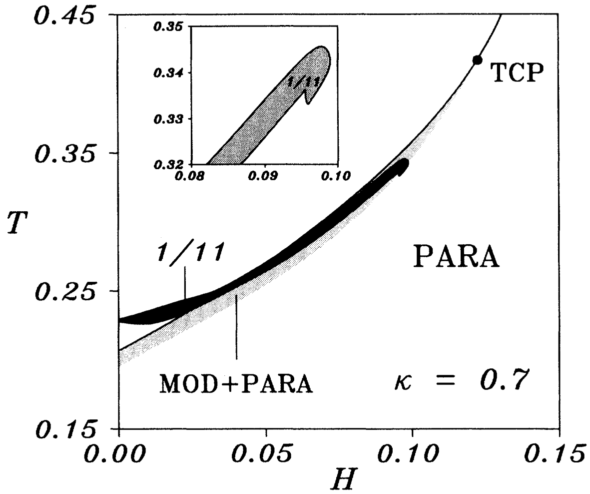

FIG. 19. 1/11 phase for $\kappa = 0.7$ (dark-shaded region). In light-shaded region paramagnetic and modulated phases are co-stable.

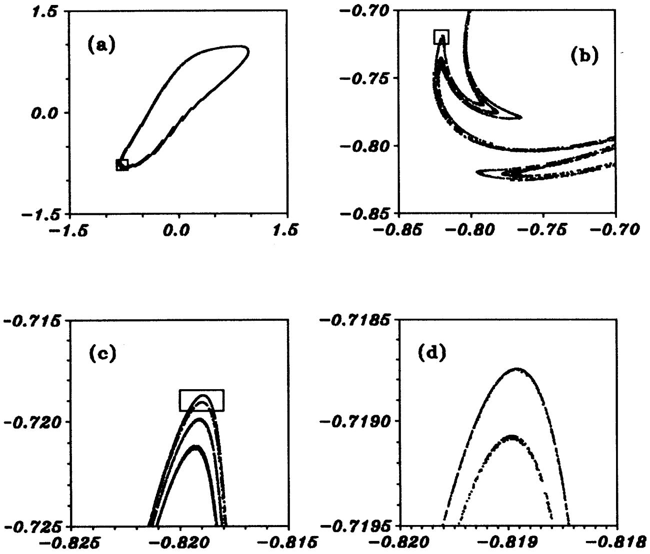

FIG. 20. Strange attractor found at $\kappa = 0.6$, $H = 0.35$, and $T = 0.0247$. Different magnifications reveal its fractal nature.

nent computed using the method of Eckmann and Ruelle [21] is $\lambda_1 = 0.049$. In these figures we have always started from the initial point $(x_1, y_2) = (1, 1)$ and disregard the 10 000 initial points. The sequence of Figs. 20(a)–20(d) shows the attractor at increasing magnifications, and we can clearly observe its fractal nature. Figures 20(a)–20(d) contain, respectively, 3000, 4000, 2500, and 730 points of the mapping, corresponding to a total of 15 000, 50 000, 200 000, and 1 000 000 iterations, respectively.

IX. CONCLUDING REMARKS

In this paper we studied the field behavior of an Ising model with competing interactions on a Bethe lattice. Although it is simpler than the ANNNI model [3], it is possible that some of the features found in the model may also be present in the ANNNI model.

We obtained detailed T-H phase diagrams for representative values of the parameter κ, which give a fairly complete picture of the commensurate phases in the T-H-κ space. This was possible using two methods that are much more powerful than the direct iteration of the mapping. These methods can also be applied to other dissipative mappings in order to determine the region of stability of periodic cycles.

Typically, commensurate phases that are present at zero field survive in the H-T phase diagram. For $\kappa < 1$ they reach fields that are quite high then fold back to terminate inside the region of co-stability of paramagnetic and modulated phases. For $\kappa > 1$, however, they terminate at the multiphase point. For $\kappa > 1$ there are, in addition to the commensurate phases already present at zero field, other commensurate phases with wave numbers less than q_c that spring up from the multiphase point and resemble the coats of an onion. In the central part of the onion-shaped region there is a co-stability of different modulated phases.

When examined closely the T-H phase diagrams exhibit great richness, which we have explored only partially. For example, distinct commensurate phases with the same wave number may be co-stable, which seems not to happen at zero field but is quite common in the presence of a field. Much more difficult to study are the regions of co-stability of different modulated phases. We limited ourselves to show that strange attractors can be found in all these regions.

ACKNOWLEDGMENTS

M.H.R.T. acknowledges financial support from Coordenação de Aperfeiçoamento de Pessoal de Nível Superior (Capes). C.S.O.Y. acknowledges partial financial support from Conselho Nacional de Desenvolvimento Científico e Tecnológico (CNPq) and Fundação de Amparo à Pesquisa do Estado de São Paulo (FAPESP).

---

[1] See, e.g., R. J. Baxter, *Exactly Solved Models in Statistical Mechanics* (Academic, London, 1982), p. 47.

[2] J. Vannimenus, Z. Phys. B **43**, 141 (1981).

[3] For recent reviews of the ANNNI model, see W. Selke, Phys. Rep. **170**, 213 (1988); J. M. Yeomans, Solid State Phys. **41**, 151 (1988).

[4] C. S. O. Yokoi, M. J. de Oliveira, and S. R. Salinas, Phys. Rev. Lett. **54**, 163 (1985).

[5] C. P. C. Prado and N. Fiedler-Ferrari, Phys. Lett. A **135**, 175 (1989).

[6] D. J. Thouless, Phys. Rev. Lett. **56**, 1082 (1986).

[7] J. M. Carlson, J. T. Chayes, L. Chayes, J. P. Sethna, and D. J. Thouless, J. Stat. Phys. **61**, 987 (1990).

[8] J. M. Carlson, J. T. Chayes, J. P. Sethna, and D. J. Thouless, J. Stat. Phys. **61**, 1069 (1990).

[9] C. E. I. Carneiro and W. F. Wreszinski, Phys. Rev. A **43**, 5691 (1991).

[10] See, e.g., A. J. Lichtenberg and M. A. Lieberman, *Regular and Stochastic Motion* (Springer-Verlag, New York, 1983).

[11] S. Aubry, in *Solitons and Condensed Matter*, edited by A. R. Bishop and T. Schneider (Springer-Verlag, Berlin, 1978).

[12] C. S. O. Yokoi, M. D. Coutinho-Filho, and S. R. Salinas, Phys. Rev. B **24**, 4047 (1981).

[13] J. Smith and J. M. Yeomans, J. Phys. C **15**, L1053 (1982).

[14] V. L. Pokrovsky and G. V. Uimin, Zh. Eksp. Teor. Fiz. **82**, 1640 (1982) [Sov. Phys.-JETP **55**, 950 (1982)].

[15] W. Selke and P. M. Duxbury, Z. Phys. B **57**, 49 (1984).

[16] A. M. Mariz, C. Tsallis, and E. L. Albuquerque, J. Stat. Phys. **40**, 577 (1985).

[17] S. Inawashiro, C. J. Thompson, and G. Honda, J. Stat. Phys. **33**, 419 (1983).

[18] J. G. Moreira and S. R. Salinas, Phys. Rev. B **47**, 778 (1993).

[19] W. H. Press, B. P. Flannery, S. A. Teukolsky, and W. T. Vettering, *Numerical Recipes* (Cambridge University Press, Cambridge, 1986).

[20] M. Feigenbaum, Los Alamos Sci. **1**, 4 (1980).

[21] J. P. Eckmann and D. Ruelle, Rev. Mod. Phys. **57**, 617 (1985).

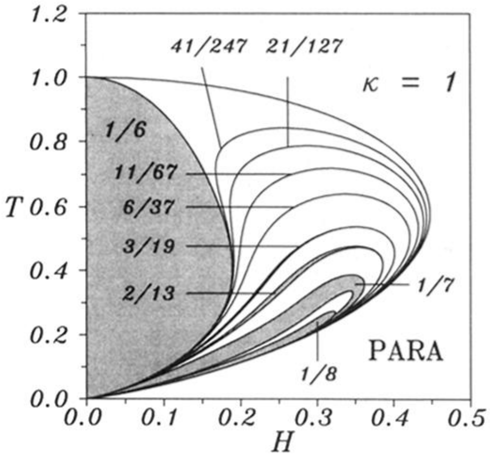

FIG. 10. T-H phase diagram for $\kappa = 1$.

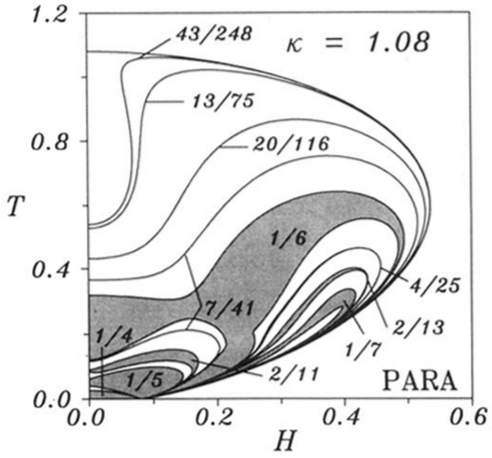

FIG. 11. *T*-*H* phase diagram for $\kappa = 1.08$.

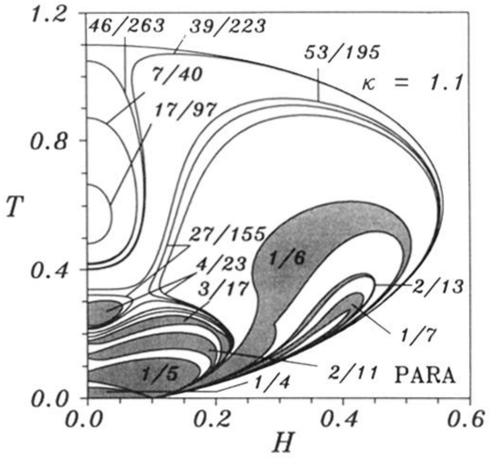

FIG. 12. T-H phase diagram for $\kappa = 1.1$.

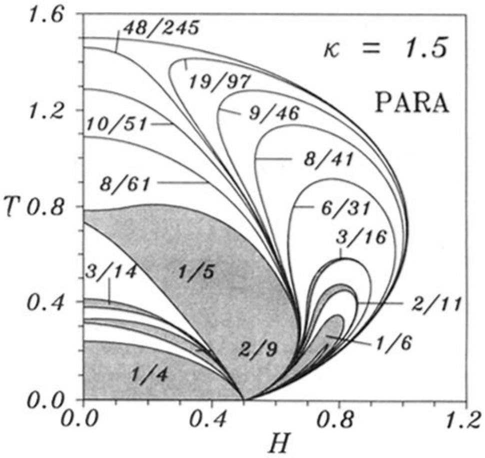

FIG. 13. T-H phase diagram for $\kappa = 1.5$.

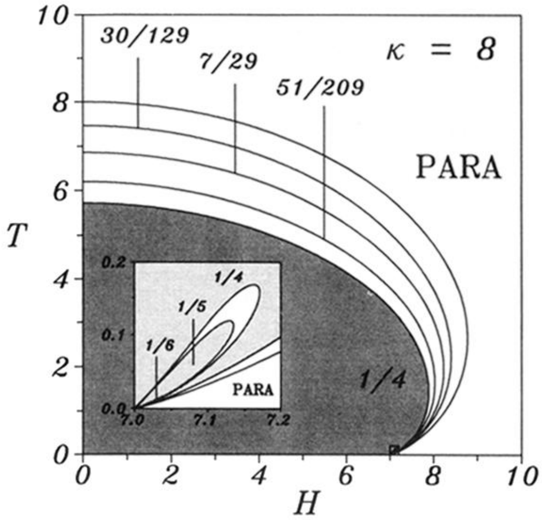

FIG. 14. T-H phase diagram for $\kappa = 8$. The inset shows the detail near the multiphase point.

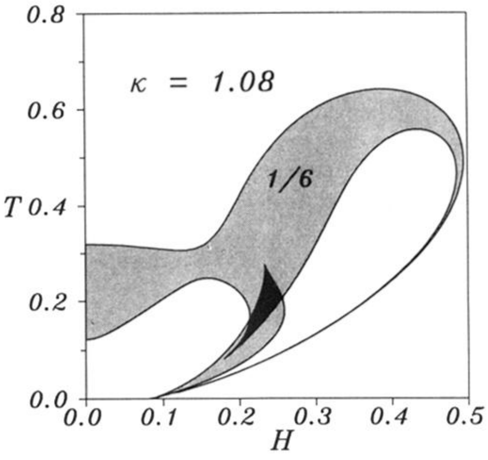

FIG. 15. Region of co-stability of different 1/6 phases (dark-shaded region) for $\kappa = 1.08$.

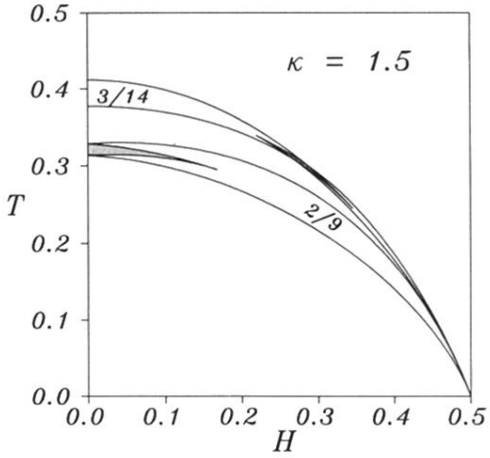

FIG. 16. Regions of co-stability of 2/9 and 3/14 phases with different structures (shaded regions).

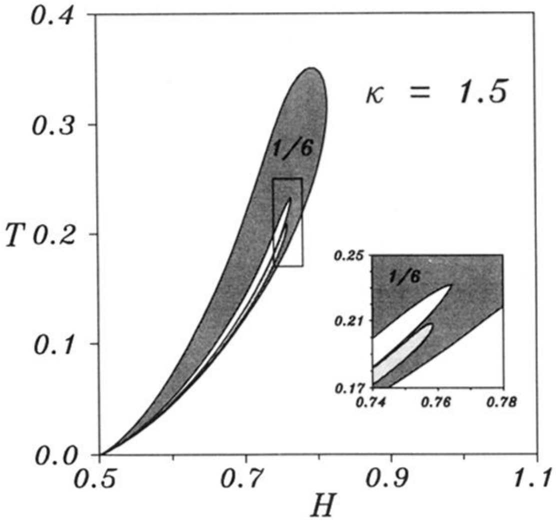

FIG. 17. Detail of the 1/6 phase for $\kappa = 1.5$. In the lighter shaded region the 1/6 phase becomes unstable.

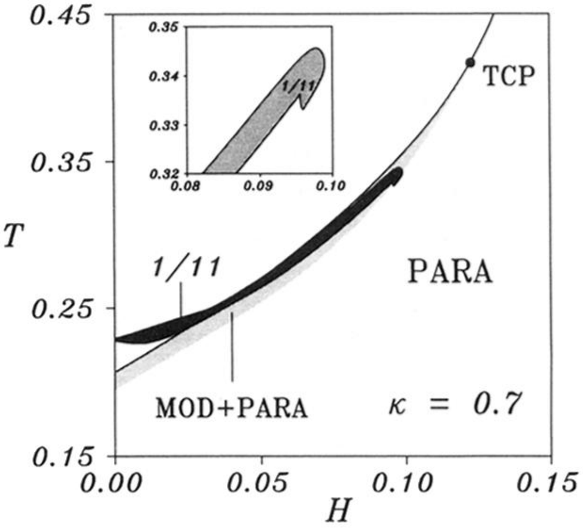

FIG. 19. 1/11 phase for $\kappa = 0.7$ (dark-shaded region). In light-shaded region paramagnetic and modulated phases are co-stable.

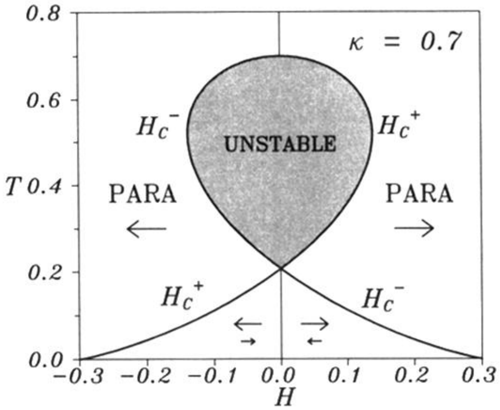

FIG. 4. Stability region of the paramagnetic phase for $\kappa = 0.7$. Inside the tent shaped region there is a co-stability of two phases, with magnetizations parallel and antiparallel to the field, as indicated by the arrows. Inside the shaded bubble-shaped region the paramagnetic phase is unstable.

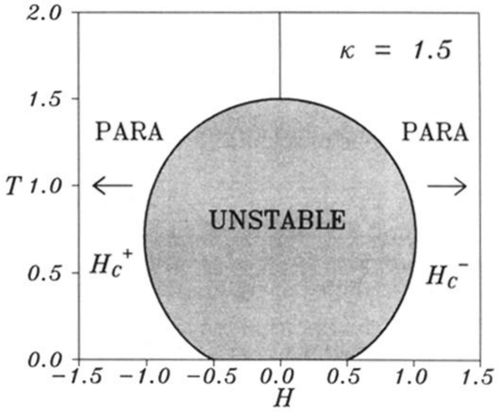

FIG. 5. Stability region of the paramagnetic phase for $\kappa = 1.5$. Inside the shaded bubble-shaped region the paramagnetic phase is unstable.

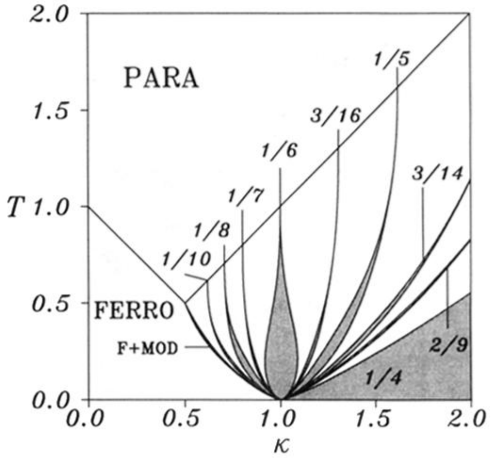

FIG. 6. Zero field T-κ phase diagram. Only the main commensurate phases (shaded regions) are indicated. In the shaded region indicated by F+MOD the ferromagnetic and modulated phases are co-stable.

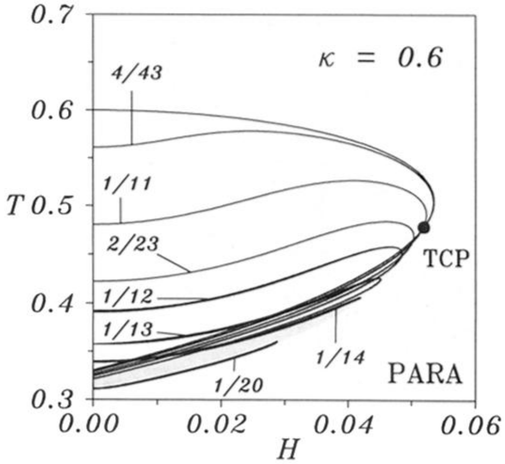

FIG. 7. T-H phase diagram for $\kappa = 0.6$. In the light-shaded region paramagnetic and modulated phases are co-stable. The co-stability region ends at the tricritical point (TCP).

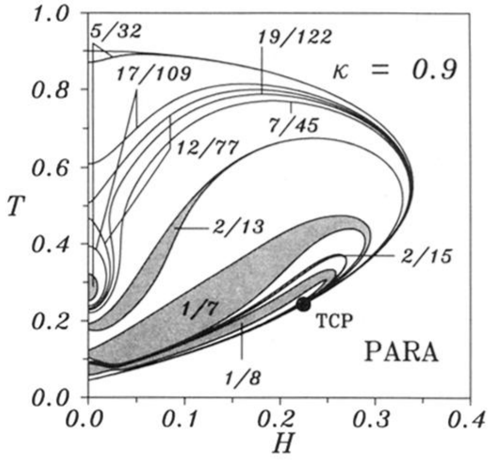

FIG. 8. T-H phase diagram for $\kappa = 0.9$. Observe the existence of disjoint commensurate phases and the pinching of the 1/8 phase. The co-stability region between paramagnetic and modulated phases is too narrow to be visible at the scale of the figure, and ends at the tricritical point (TCP).

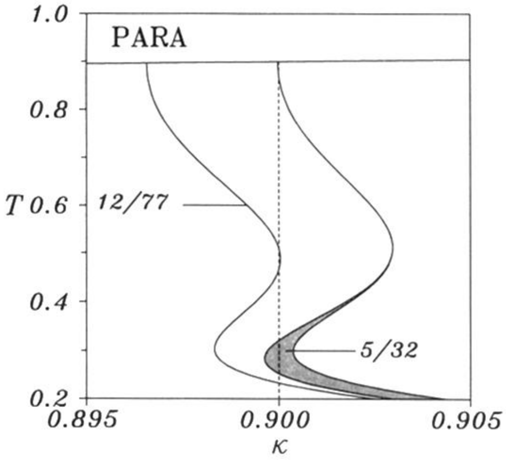

FIG. 9. Detail of the T-κ phase diagram in the neighborhood of $\kappa = 0.9$. The phases 5/32 and 12/77 recur two and three times, respectively, as the temperature is lowered for $\kappa = 0.9$.